ECOM-74-0470-3

SYSTEMATIC STUDY OF PYROELECTRICITY

Light Scattering and Pyroelectricity in Ferroelectrics

M. I. Bell and P. M. Raccah
Yeshiva University
Belfer Graduate School of Science
2495 Amsterdan Avenue
New York, New York 10033

April 1976

Interim Report for Period 1 April 1975 - 30 September 1975

Sponsored by

ADVANCED RESEARCH PROJECTS AGENCY
1400 Wilson Blvd.
Arlington, VA 22209
ARPA Order No. 2573

US Army Electronics Command
Fort Monmouth, NJ 07703

NOTICES

Disclaimers

The findings in this report are not to be construed as an official Department of the Army position, unless so designated by other authorized documents.

The citation of trade names and names of manufacturers in this report is not to be construed as official Government indorsement or approval of commercial products or services referenced herein.

Disposition

Destroy this report when it is no longer needed. Do not return it to the originator.

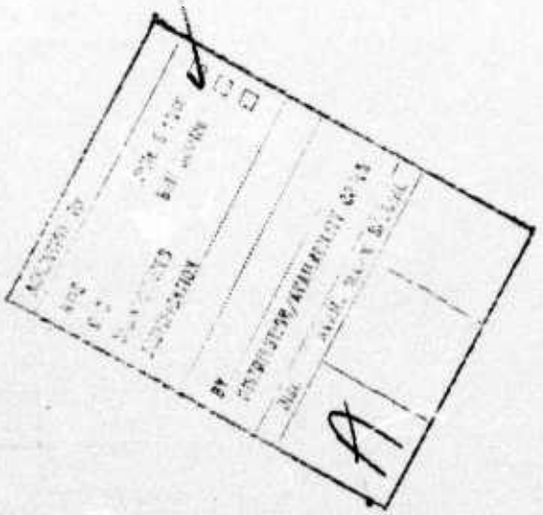

UNCLASSIFIED

SECURITY CLASSIFICATION OF THIS PAGE *(When Data Entered)*

(18) (19) **REPORT DOCUMENTATION PAGE**

READ INSTRUCTIONS BEFORE COMPLETING FORM

1. REPORT NUMBER	2. GOVT ACCESSION NO.	3. RECIPIENT'S CATALOG NUMBER
ECOM-74-0470-3		

(6) 4. TITLE (and Subtitle)
SYSTEMATIC STUDY OF PYROELECTRICITY. Light Scattering and Pyroelectricity in Ferroelectrics.

(9) 5. TYPE OF REPORT & PERIOD COVERED
Technical Report. 1 Apr [redacted] -30 Sep [redacted] 75.

6. PERFORMING ORG. REPORT NUMBER

(10) 7. AUTHOR(s)
M.L.Bell [redacted] P.M.Raccah

(15) 8. CONTRACT OR GRANT NUMBER(s)
DAAB 07-74-C-0470, ✓ARPA Order - 2573

9. PERFORMING ORGANIZATION NAME AND ADDRESS
Yeshiva University, Belfer Graduate School of Science, 2495 Amsterdam Ave., New York, N.Y. 10033

10. PROGRAM ELEMENT, PROJECT, TASK AREA & WORK UNIT NUMBERS
Program Code No. 4010

11. CONTROLLING OFFICE NAME AND ADDRESS
Advanced Research Projects Agency
1400 Wilson Blvd.
Arlington, VA 22209

(11) 12. REPORT DATE
Apr [redacted] 76

13. NUMBER OF PAGES
38

14. MONITORING AGENCY NAME & ADDRESS *(if different from Controlling Office)*
US Army Electronics Command
Fort Monmouth, NJ 07703 DRSEL-TL-ES

15. SECURITY CLASS. *(of this report)*
Unclassified

15a. DECLASSIFICATION/DOWNGRADING SCHEDULE

16. DISTRIBUTION STATEMENT *(of this Report)*

Approved for public release; distribution unlimited

(12) 43p.

17. DISTRIBUTION STATEMENT *(of the abstract entered in Block 20, if different from Report)*

18. SUPPLEMENTARY NOTES

This research was supported by Advanced Research Projects Agency of the Department of Defense and was monitored by US Army Electronics Command under Contract No. DAAB-07-74-C-0470

(see reverse side)

19. KEY WORDS *(Continue on reverse side if necessary and identify by block number)*

Ferroelectrics, Pyroelectric detectors, Figure of merit, Phase transitions, Molecular field theory, Triglycine sulfate, Potassium niobate, Raman scattering, vidicons

20. ABSTRACT *(Continue on reverse side if necessary and identify by block number)*

The results of two studies of pyroelectric materials are reported. In the first, a Raman scattering study of $KNbO_3$, anomalous scattering is found which can be related directly to the dynamic disorder which has been invoked to explain the results of earlier x-ray and neutron scattering studies and which provides the starting point for the generalized molecular field theory of ferroelectricity proposed elsewhere by the authors. The second is an analysis of the physical properties of pyroelectric materials which determine their performance as vidicon targets. The role of thermal diffusion is assessed and

DD FORM 1 JAN 73 1473 EDITION OF 1 NOV 65 IS OBSOLETE

053 820

UNCLASSIFIED

SECURITY CLASSIFICATION OF THIS PAGE *(When Data Entered)*

18. Supplementary Notes (cont'd)

ARPA Contractor: Yeshiva University
P.M. Raccah, Principal Investigator
(212) 568-8400

Project Scientists: FREDERICK ROTHWARF, (201) 544-4407
GERALD J. IAFRATE (201) 544-4070

20. Abstract (cont'd)

found to be independent of the dielectric parameters which determine the signal-to-noise figure of merit. Examination of the figures of merit relevant to vidicon operation in the anode potential stabilized and cathode potential stabilized modes shows that among proper ferroelectrics substantial (i.e. order-of-magnitude) improvement over presently available materials is impossible in the first case and highly unlikely in the second.

CONTENTS

I. INTRODUCTION

The work described in this report was conducted from 1 April 1975 to 30 September 1975 under Advanced Research Projects Agency contract DAAB 07-74-C-0470, P.M. Raccah, principal investigator, F. Rothwarf and G. Iafrate, contract monitors. The purpose of this investigation is to elucidate the physical mechanism responsible for the pyroelectric effect and to assess the extent to which this effect can be exploited in the construction of infrared detectors and imaging devices. In previous reports and publications we have proposed[1,2] and elaborated on[3] a generalized molecular field theory (GMFT) of ferroelectricity and pyroelectricity which provides a quantitative basis for study of those pyroelectric materials which are also ferroelectric. An underlying assumption of the GMFT is the existence of elementary dipoles which persist (although in a disordered state) at temperatures well above the ferroelectric-to-paraelectric transition, even in so-called displacement ferroelectrics. In the spring of 1974, an experimental study of $KNbO_3$, a typical displacement ferroelectric, was begun in collaboration with A.M. Quittet and M. Lambert in order to determine whether effects attributable to the presence of such dipoles could be observed in the Raman scattering spectra. This proved indeed to be the case, and preliminary results were reported at a meeting of the American Physical Society[4]. To complete the experimental picture, especially with respect to the temperature dependence of the Raman spectra, further studies were made in collaboration with M. Krauzman, and Section II of this report consists of a paper describing this work which has been submitted to Solid State Communications. The detailed results presented there fully confirm the preliminary findings[4] and provide further evidence for the validity of the assumptions on which the GMFT is based.

With respect to the use of pyroelectric materials in infrared detection, our earlier work[1,5] had shown that both the GMFT and more fundamental thermodynamic arguments could be used to study the signal-to-noise figures of merit of pyroelectric materials used in small-area detectors and vidicons. A detailed treatment of the vidicon case was carried out, and the results were discussed in a paper[6], presented to the 1975 International Electron Devices Meeting and reproduced as Section III of this report. This study concluded that while the thermal diffusivity of the target material plays a significant role in determining vidicon performance, this parameter can be treated independently of the figure of merit, and improved performance can be obtained by selecting a material with a low Debye temperature. More significantly, quantitative predictions of the figures of merit of pyroelectric materials in vidicon applications were obtained. Different figures of merit are relevant to the two commonly used modes of vidicon operation, anode potential stabilization (APS) and cathode potential stabilization (CPS). For the APS mode we were able to show, using purely thermodynamic arguments, that an upper bound exists for the figure of merit which is only a factor 2.5 greater than the largest value yet obtained experimentally. In the CPS case, the GMFT was used with extreme but still physically reasonable values of its parameters, chosen to give the largest possible figure of merit. The result was only a factor of three greater than the best value currently available. The CPS result is subject of course to any limitations which may exist to the validity of the GMFT. It is restricted, for example, to so-called proper ferroelectrics, in which the polarization is the order parameter of the

ferroelectric phase transition. Improper ferroelectrics, in which the spontaneous polarization arises indirectly, via a coupling to the actual order parameter, may yield higher values of this figure of merit than are predicted by the GMFT and are well worth investigating from that point of view.

References

1. M.I. Bell and P.M. Raccah, Technical Report ECOM-74-0470-1, Yeshiva University (1975).
2. M.I. Bell and P.M. Raccah, Bull. Am. Phys. Soc. 20, 349 (1975).
3. M.I. Bell and P.M. Raccah, Technical Report ECOM-74-0470-2, Yeshiva University (1975).
4. A.M. Quittet, M.I. Bell, M. Lambert, and P.M. Raccah, Bull. Am. Phys. Soc. 20, 327 (1975).
5. M.I. Bell and P.M. Raccah, unpublished.
6. M.I. Bell and P.M. Raccah, IEDM Tech. Digest, 70 (1975).

II. ANOMALOUS SCATTERING AND ASYMMETRICAL LINE SHAPES IN RAMAN SPECTRA OF ORTHORHOMBIC $KNbO_3$

by

A. M. Quittet

Laboratorie de Physique des Solides

Universite Paris-Sud, Orsay

M. I. Bell

Physics Department

Yeshiva University

New York, New York

M. Krauzman

Département de Recherches Physiques

Laboratoire Associé au CNRS No. 71

Université, Paris VI

and

P. M. Raccah

Physics Department

Yeshiva University

New York, New York

ABSTRACT

The Raman spectrum of orthorhombic $KNbO_3$ is found to contain anomalous scattering, consisting of a large background and broad bands, which can be related directly to the dynamic disorder which has been invoked to explain the results of earlier studies of diffuse x-ray scattering and inelastic neutron scattering. Some ordinary first order lines exhibit coupling to the anomalous part of the spectrum which is revealed by the existence of resonant interference of the type described by Fano. All these features disappear abruptly at the transition to the low-temperature, rhombohedral phase, indicating that they are characteristic of the peculiar dynamics of linear chains observed in the orthorhombic, tetragonal, and cubic phases.

INTRODUCTION

In the ferroelectric perovskites such as $BaTiO_3$ and $KNbO_3$, x-ray diffuse scattering[1] and inelastic neutron scattering[2,3] experiments yield evidence of a very large anisotropy in the dispersion of some of the vibrational modes. Light scattering[4,5] has been used to investigate the zone-center phonons in order to check the soft mode theories[6]. We report here some new results of Raman scattering experiments performed on a single-domain $KNbO_3$ sample, both in its room temperature orthorhombic phase and as the temperature is lowered through the orthorhombic to rhombohedral phase transition.

The assignment of the ordinary first order lines is quite easily obtained, leaving outside this classification a large continuous scattering which we refer to as "anomalous". The latter, previously described in Ref. 5 for restricted scattering geometries, has now been found to occur more generally whenever the incident and scattered beams propagate perpendicular to the Z-axis and are simultaneously polarized parallel to Z. As expected, this anomalous spectrum disappears abruptly at the orthorhombic to rhombohedral transition temperature, as does the normal low frequency $B_2(TO)$ line. In the spectra where the anomalous scattering occurs, some first order lines display an asymetrical shape characteristic of a "Fano interference"[7].

EXPERIMENTAL

The Raman scattering was excited by an argon-ion laser operating at either 4880 Å or 5135 Å. Measurements were made using a ½-meter Spex double grating spectrometer located at the Maybaum Institute of Yeshiva University and a Codberg T800 triple grating spectrometer located at Département de Recherches Physiques, Université Paris VI. Both systems

employed photon counting detection.

We used a single-domain sample cut with the faces perpendicular to the orthorhombic axes. Standard right-angle and back-scattering geometries were used to obtain various linear momentum transfers from the photons to the crystals. Table I summarizes the modes which can be observed in each scattering geometry. The orthorhombic axes are related to the pseudocubic ones as described in Fig. 1. At zero wavevector, the irreducible representations of the 12 optic modes in the C_{2v} point group of the orthorhombic phase are as follows: 4 $A_1(X)$, 4 $B_1(Y)$, 3 $B_2(Z)$, 1 A_2. All A_1, B_1 and B_2 modes are infrared active (the letters in parentheses indicate the direction of the dipole moment of each mode), and for these the longitudinal or transverse character must be considered. Two features of this table should be noted. First, B_1 and B_2 modes are not detected in a longitudinal configuration. Second, when a polar mode is neither transverse nor longitudinal in a given scattering geometry (labelled "mixed"), it looses its zero wavevector irreducible representation species through mixing with modes of different symmetry.

ROOM TEMPERATURE SPECTRA

All the spectra listed in Table I have been recorded. Only those of special interest are reproduced in Figures 2 and 3. In Fig. 2, the peaks which arise from contamination by other species are drawn with broken lines.

From Table I, and taking into account the possible mixing of species, we can assign the observed frequencies to the different modes. These assignments are summarized in Table II. Within the limit of experimental accuracy, we agree with the results published independently by Winter et al[5], at least for those lines identified unabiguously in Ref. 5. The following details should be noted. The low frequency $B_2(TO)$ line (maximum at 40 cm^{-1}) is broad and asymetrical (Fig. 2a), and a thin line at 195 cm^{-1} which sits

on its tail is slightly distorted and seems to show a dip on the low frequency side. In the B_2 mixed spectrum, the lines at 170 and 205 cm^{-1} display an interference dip between them (Fig. 2b).

The anomalous spectrum is seen in the following geometries: $Y(ZZ)\bar{Y}$, $X(ZZ\bar{X}$ and $X(ZZ)Y$. These are $A_1(TO)$, $A_1(LO)$, and A_1(mixed) spectra, respectively, and are shown in Fig. 3e, a, c. In each case, the linear momentum transfer is perpendicular to the Z axis, and the light beams are polarized parallel to Z. The anomalous scattering, identical in the three spectra, consists of a continuous background, decreasing in intensity from low to high frequency, and two broad bumps centered near 130 and 430 cm^{-1}.

The ordinary first order lines are superimposed on the anomalous spectrum,but some of them show a coupling leading to an asymetrical lineshape and interference dip. This is clearly demonstrated by comparison of the pairs of spectra in Fig. 3:

i) Fig. 3a and 3b: The normal $X(YY)\bar{X}$ spectrum together with the anomalous $X(ZZ)\bar{X}$ one are both $A_1(LO)$ spectra. Note the lines at 195 and 435 cm^{-1}.

ii)Fig. 3d and 3e: The normal $Y(XX)\bar{Y}$ spectrum together with the anomalous $X(ZZ)\bar{Y}$ one are both $A_1(TO)$ spectra. Note the line at 193 cm^{-1}.

iii)Fig. 3c: The anomalous $X(ZZ)Y$ spectrum has A_1(mixed) symmetry. Note the mode at 420 cm^{-1} which appears almost wholly negative in the anomalous part of the spectrum.

TEMPERATURE DEPENDENCE[8] ($23^{o}C$ to $-70^{o}C$)

As the temperature is lowered, there is essentially no change in the low frequency $B_2(TO)$ line and the anomalous spectrum until the transition temperature is reached. The frequency and width of the B_2 line both

decrease slightly, but its intensity (Fig. 4a), as well as the shape and intensity of the anomalous spectrum,remains unchanged. Below the phase transition, which takes place near -59°C, the spectrum becomes very different (Fig. 4b, c) as the broad B_2 line and the anomalous scattering disappear completely. Since the sample becomes broken and twinned, all the spectra are superimposed, so that it is not possible to miss any lines. Upon reheating the sample, the anomalous spectra of the orthorhombic phase appear again at -30°C, exhibiting the large thermal hysteresis characteristic of a first order transition. These experiments thus demonstrate that the anomalous spectrum is related to an intrinsic property of the orthorhombic phase, as is the low frequency B_2(TO) line.

DISCUSSION

We note first that all the anomalous features which appear in Raman, neutron, and x-ray scattering experiments occur only when the linear momentum transfer lies perpendicular to the Z-axis, and that these features disappear in the rhombobedral phase. Hence the dynamical properties of the orthorhombic phase have a pronounced one-dimensional character. These results can be understood[1] as arising from displacements of the niobium atoms in the Z direction (away from the C_2 symmetry axis) which are correlated for some finite distance along Z. Averaged over distances large compared to this correlation length, however, the structure retains orthorhombic symmetry. Such disorder need not be static, since its effects will be seen in scattering experiments provided the lifetime of the local departure from the average symmetry is greater than the scattering time. From this point of view, the anomalous features in the Raman spectra can be interpreted as disorder-induced first-order scattering, i.e. one-phonon scattering by modes which would not be Raman active in a

perfect crystal but which become so when both the translational and point-group symmetries are broken by the disorder. Since all phonons (not only those at the zone center) can become Raman active in this way, one anticipates a scattering spectrum proportional, in first approximation, to the one-phonon density of states. This interpretation is further strengthened by the fact that neutron scattering results[3] suggest the existence of a peak in the one-phonon density of states near 150 cm^{-1}, close to one of the peaks (130 cm^{-1}) in the anomalous Raman spectra.

We have studied the modification of the spectra which occurs as the linear momentum transfer is rotated from the Y direction to the Z direction. As the momentum transfer is changed, the intensity of the anomalous scattering decreases rapidly, while the frequency of the B_2 line shifts very rapidly toward higher values (Fig. 5a,b). We conclude from this that the B_2 line is produced by an underdamped zone-center phonon with a large LO-TO frequency difference and that the anomalous spectrum in ZZ polorization arises from a continuum of states. Our identification of the line at 40 cm^{-1} as the zone-center B_2(TO) phonon is consistent with the results of neutron scattering experiments.[3] Although Currat et al[3] extrapolate the frequency of the optical branch to about 25 cm^{-1} at the zone center, the experimental resolution is such that spectra near the zone center and at low frequencies are always heavily contaminated by the Bragg peak and the acoustic dispersion. Moreover, the experimental points closest to the zone center could only be obtained from constant energy scans which do not provide an accurate measure of mode frequency.

The asymmetrical line shapes observed in this work are of two types.

One is produced by the small interference between the two lowest-lying lines in the B_2(TO) spectrum (Fig. 2a). This is merely a coupling between modes of identical symmetry, which appears because of the large width of the low-frequency line. The coupling becomes much stronger when the wavevector is rotated 45° from the Y axis toward the Z axis, since the rapid increase in the frequency of the lower mode brings the two modes quite close (Fig. 2b).

The second type of asymmetry can be seen in the shape of several narrow lines observed in the anomalous ZZ spectra. This can be analyzed, using a formalism developed by Fano[7], as an interference between the scattering by a discrete, one-phonon state and a continuum of states. Such line shapes have been reported previously in $BaTiO_3$ by Rousseau and Porto[9] and in heavily doped silicon by Cerdeira et al[10]. The application of Fano's formalism to Raman scattering has been treated in detail by Scott[11]. If the Hamiltonian H couples a discrete state φ with a continuum ψ_E according to

$$\begin{aligned} \langle \varphi \,|H|\, \varphi \rangle &= E_{\varphi} \\ \langle \psi_E \,|H|\, \varphi \rangle &= V_E \\ \langle \psi_{E'} \,|H|\, \psi_E \rangle &= E\ \delta(E-E'), \end{aligned} \tag{1}$$

then the observed scattering cross section σ is related to the cross section σ_E which would be produced by the continuum in the absence of any coupling by

$$\sigma = \frac{(q+\epsilon)^2}{1+\epsilon^2}\ \sigma_E\ . \tag{2}$$

Here $\epsilon = (E - E_\varphi - \delta E)/\Gamma$ is a reduced energy variable involving the half-width $\Gamma = \pi|V_E|^2$ and energy shift $\delta E = \pi^{-1}\mathcal{P}\int dE'\Gamma/(E-E')$ ($\mathcal{P}$ indicates "principal part of") of the "resonant" state resulting from the discrete-continuum interaction. The parameter $q = (\pi V_E)^{-1} \langle \Phi|\alpha_{ij}|i\rangle/\langle\psi_E|\alpha_{ij}|i\rangle$ depends on the matrix elements of the Raman tensor α_{ij} for transitions from an initial state $|i\rangle$ to the continuum ψ_E and to the state $\Phi = \varphi + \mathcal{P}\int dE'\ V_{E'}\psi_{E'}/(E-E')$, which is the discrete state φ modified by an admixture of continuum states. If q and Γ are independent of E in a sufficiently large interval around E_φ, the spectrum can be fitted to Eq. (2) with q and Γ treated as (energy-independent) fitting parameters. (Note that Γ and q cannot be completely independent of energy unless $\delta E = 0$.) Figure 6 compares the experimental $X(ZZ)\bar{X}$ spectrum near 430 cm^{-1} with the prediction of Eq. (2) to which a slowly varying background has been added. A good fit is obtained for $q = 0.75$, $\Gamma = 3.6$ cm^{-1}, $E_\varphi + \delta E = 432.7$ cm^{-1}. The value of E_φ obtained from the $X(YY)\bar{X}$ spectrum (Fig. 3b) is 430 cm^{-1}, yielding a shift $\delta E = 2.7$ cm^{-1} due to the coupling. The exact nature of this coupling remains to be determined. If, as we have proposed, the continuum is produced by disorder-induced first-order scattering, it may be coupled to zone-center modes via anharmonic terms in H as discussed by Scott[11] or via additional terms which depend directly on the disorder.

CONCLUSION

The experiments described here demonstrate that a major part of the dynamical behavior of orthorhombic $KNbO_3$ is one-dimensional in character and consistent with the formation of linear chains of correlated displacements of niobium ions as proposed in connection with diffuse x-ray scattering

results[1] and Raman scattering studies of the cubic and tetragonal phases[5]. This further evidence of disorder in the orthorhombic phase, together with the observation that the lowest B_2(TO) mode does not display any significant softening with decreasing temperature, strongly suggests that the phase transitions of $KNbO_3$ (including the ferroelectric-paraelectric one) have some order-disorder character. Such a suggestion is not inconsistent with the fact that the transitions are thermodynamically of first order, since recent studies[12] of systems of dipoles interacting via a generalized molecular field have shown that first-order transitions are possible in such a model and that an accurate quantitative description of the cubic-tetragonal transition in $BaTiO_3$ can be obtained.

ACKNOWLEDGMENTS

We are indebted to Mr. Fluckinger of the Laboratorium für Festkörperphysik, ETH Zurich who provided us with the excellent single-domain $KNbO_3$ sample, to Prof. M. Lambert for helpful discussions, and to Mr. Hamel for technical assistance. The work at Yeshiva University was supported by the Advanced Research Projects Agency.

References

1. M. Lambert and R. Comes, Solid St. Comm. 7, 305 (1969).
2. A.C. Nunes, J. D. Axe, and G. Shirane, Ferroelectrics 2, 291 (1971).
3. R. Currat, R. Comes, B. Dorner, and E. Wiesendanger, J. Phys. C 7, 2521 (1974).
4. M. P. Fontana and M. Lambert, Solid St. Comm. 10, 1 (1972); M. DiDomenico, Jr., S. H. Wemple, S. P. S. Porto, and R. P. Bauman, Phys. Rev. 174, 522 (1968); D. Heiman andS. Ushioda, Phys. Rev. B 9, 2122 (1974).
5. A. M. Quittet, M. Fontana, M. Lambert, and E. Wiesendanger, Ferroelectrics 8, 585 (1974); F. X. Winter, E. Wiesendanger, and R. Claus, Phys. Stat. Sol.(b) 64, 95 (1974).
6. P. Anderson, Proceedings All-Union Conference on the Physics of Dielectrics (Acad. Sci. USSR, Moscow, 1958), p. 209; W. Cochran, Adv. Phys. 9, 387 (1960); 10, 401 (1961).
7. U. Fano, Phys. Rev. 124, 1866 (1961).
8. Similar results have been reported recently by M. P. Fontana and C. Razzetti, Solid St. Comm. 17, 377 (1975).
9. D. L. Rousseau and S. P. S. Porto, Phys. Rev. Letters 20, 1354 (1968).
10. F. Cerdeira, T. A. Fjeldly, and M. Cardona, Phys. Rev. B 8, 4734 (1973).
11. J. F. Scott, Phys. Rev. Letters 24, 1107 (1970); Revs. Mod. Phys. 46, 83 (1974).
12. M. I. Bell and P. M. Raccah,Bull. Am. Phys. Soc. 20, 349 (1975); Technical Report ECOM-74-0470-1, Yeshiva University (1975).

TABLE CAPTIONS

Table I. Summary of the scattering geometries employed and the mode symmetries observed. Scattering geometries are indicated by the conventional notation $\vec{k}_i(\vec{e}_i\ \vec{e}_s)\ \vec{k}_s$, where $\vec{k}_i, \vec{e}_i$ $(\vec{k}_s, \vec{e}_s)$ are the wavevector and polarization vector of the incident (scattered) photon.

Table II. Frequencies and symmetry assignments of first-order Raman lines of $KNbO_3$. The figure in parentheses is the full width of the line at half maximum.

TABLE I

	Incident wave vector $\vec{k}_i$	Scattered wave vector $\vec{k}_s$	Momentum transer $\vec{k}_s - \vec{k}_i$	Polarization of incident and scattered beams ($\vec{\epsilon}_i \vec{\epsilon}_s$) and mode symmetry: XX (A_1)	YY (A_1)	ZZ (A_1)	YX, XY (B_1)	ZX, XZ (B_2)	YZ, ZY (A_2)
right-angle scattering	X	Y	$\perp Z$	--	--	mixed	mixed	TO	indiff.
	Y	Z	$\perp X$	TO	--	--	mixed	mixed	indiff.
	X	Z	$\perp Y$	--	mixed	--	TO	mixed	indiff.
Back scattering	X	$\bar{X}$	$\parallel X$	--	LO	LO	--	--	indiff.
	Y	$\bar{Y}$	$\parallel Y$	TO	--	TO	--	--	------
	Z	$\bar{Z}$	$\parallel Z$	TO	TO	--	TO	--	------

TABLE II

A_1(TO)	A_1(LO)	B_1(TO)	B_2(TO)	A_2
			40 (27x2)	
193 (2)	194.5 (3)	192 (2)	196.5*	
		249 (25)		
		270		
281.5 (33)				282 (6)
	295 (5)			
297 (5)				
	434.5* (10)			
			513 (20)	
		534 (20)		
606.5 (33)				
	834 (27)			

* Lines showing an asymmetrical shape in at least one scattering geometry.

FIGURE CAPTIONS

Fig. 1. Orthorhombic axes for $KNbO_3$ and corresponding pseudocubic axes (in brackets). Also shown are the symmetry elements of the C_{2v} point group. The spontaneous polarization is in the X direction.

Fig. 2. B_2 symmetry spectra: a) B_2(TO) in back-scattering geometry, b) B_2 (mixed) in right-angle geometry. The dashed lines indicate contamination from other symmetry species due either to a small misorientation of the polarizers or to mixing of polar modes as described in the text.

Fig. 3. Anomalous spectra and the associated normal spectra. In the $Y(XX)\bar{Y}$ and $Y(ZZ)\bar{Y}$ spectra, the broad line in the vicinity of 50 cm^{-1} is most probably a contamination from the $Y(XZ)\bar{Y}$ B_2(TO) spectrum due to the divergence of the scattered beam.

Fig. 4. Temperature dependence of part of the $B_1 + B_2$ spectrum: a) in the orthorhombic phase just above the phase transition (temperature decreasing), b) in the rhombohedral phase just below the transition (temperature decreasing), c) in the rhombohedral phase in the hysteresis interval (temperature increasing).

Fig. 5. a) B_2 spectrum for a momentum transer rotated by 15° from a TO configuration toward the LO configuration. b) Anomalous spectrum for the same momentum transfer.

Fig. 6. Comparison of the experimental $X(ZZ)\bar{X}$ spectrum (solid curve) with the prediction of Eq. (2) (dots).

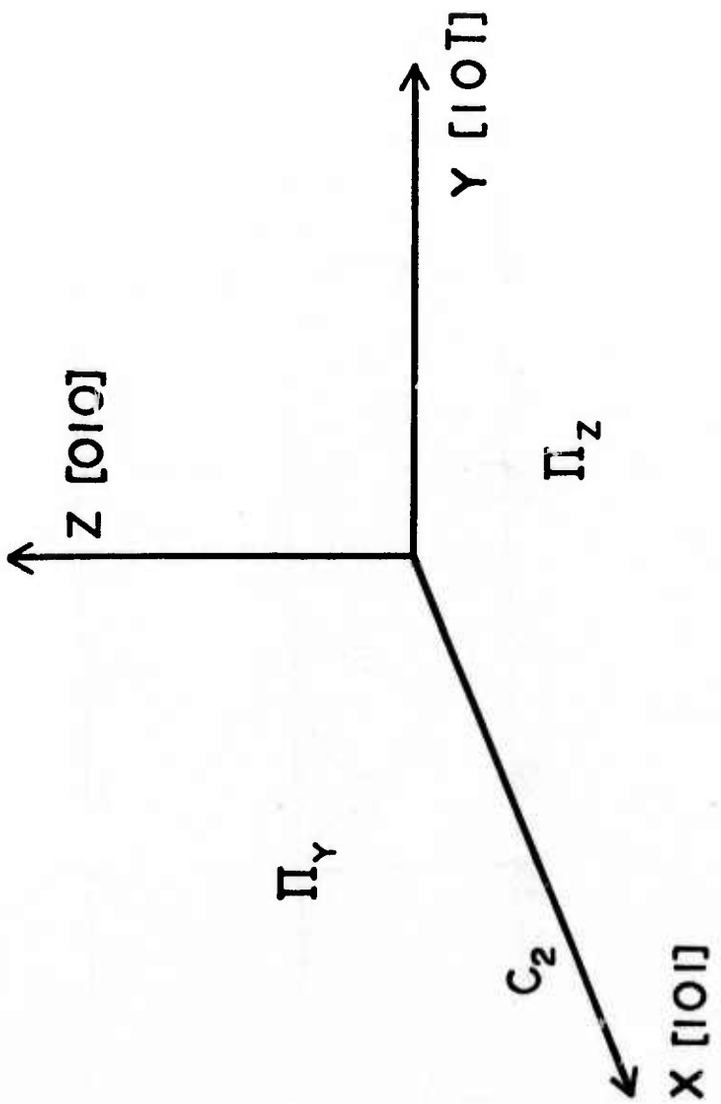

Fig. 1

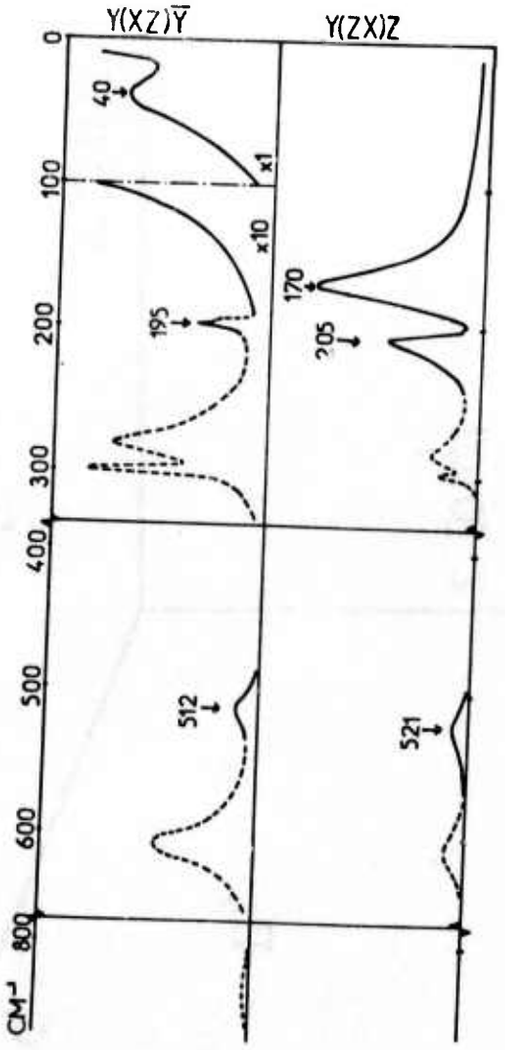
Y(XZ)$\bar{Y}$
Y(ZX)Z
0
100
200
300
400
500
600
800
CM^{-1}
40
x1
x10
195
170
205
512
521

Fig 2 (a,b)

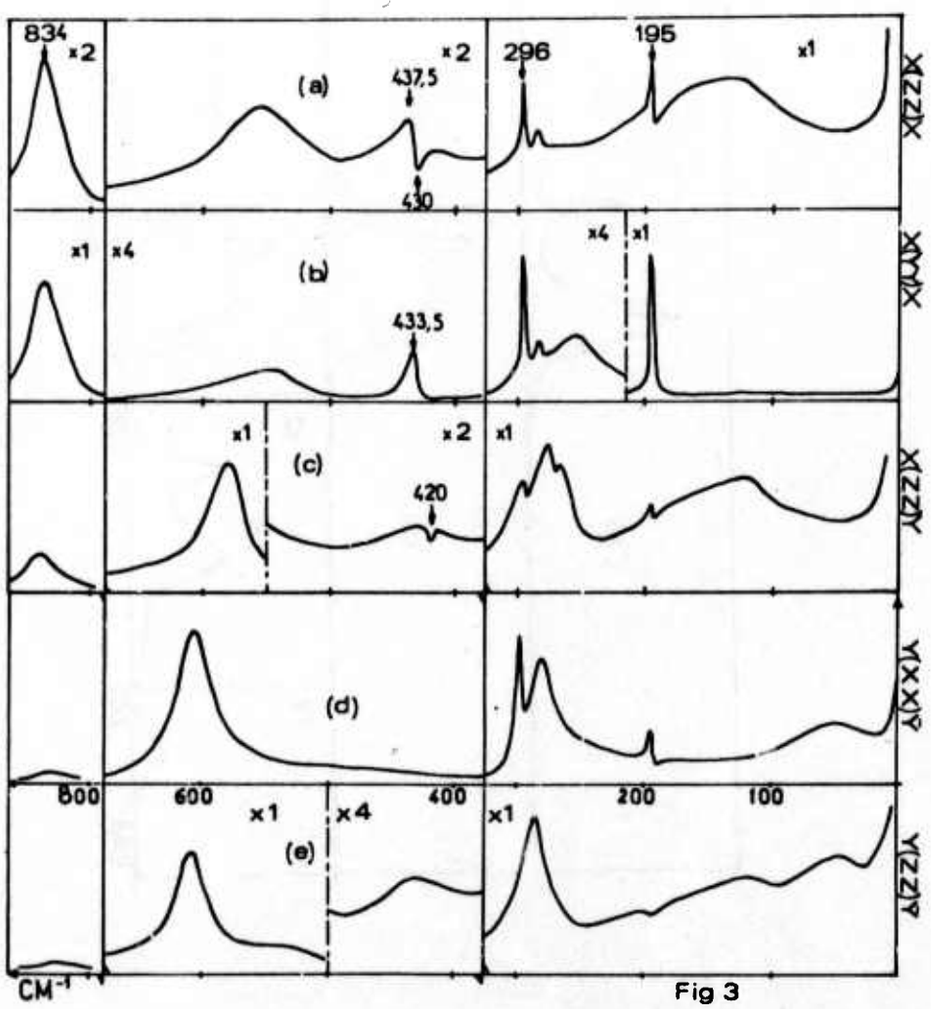
834
x2
x2
(a)
437,5
430
296
195
x1
X(ZZ)X
x1
x4
(b)
433,5
x4
x1
X(YY)X
x1
x2
(c)
420
x1
X(ZZ)Y
(d)
Y(XX)Y
800
600
x1
x4
400
200
100
(e)
x1
Y(ZZ)Y
CM-1

Fig 3

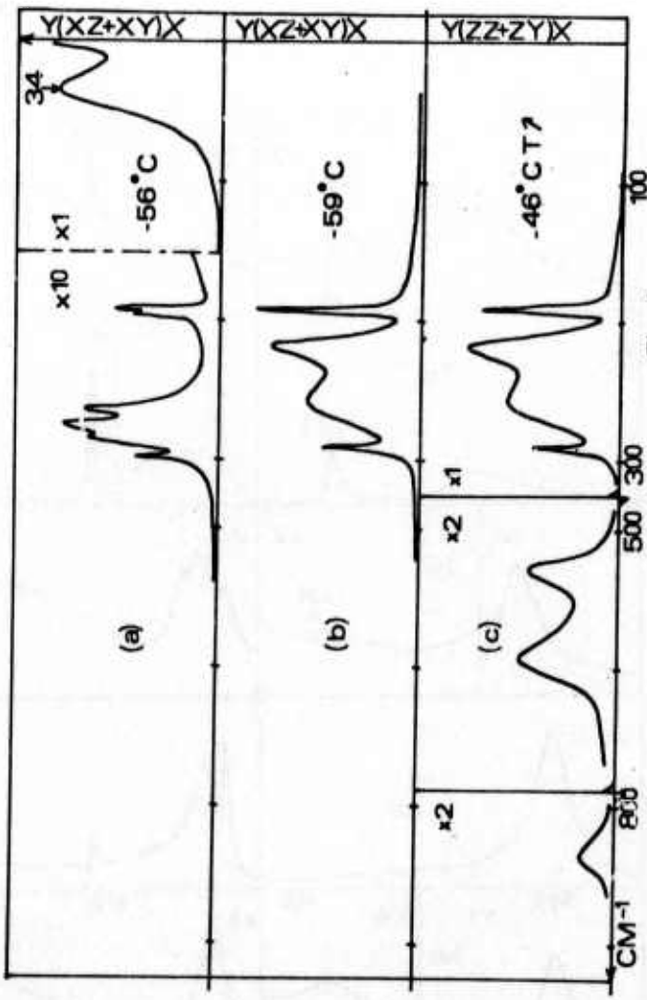
Y(XZ+XY)X
Y(XZ+XY)X
Y(ZZ+ZY)X
34
x1
x10
-56°C
-59°C
-46°C T?
100
300
500
800
x1
x2
x2
(a)
(b)
(c)
CM-1

Fig 4

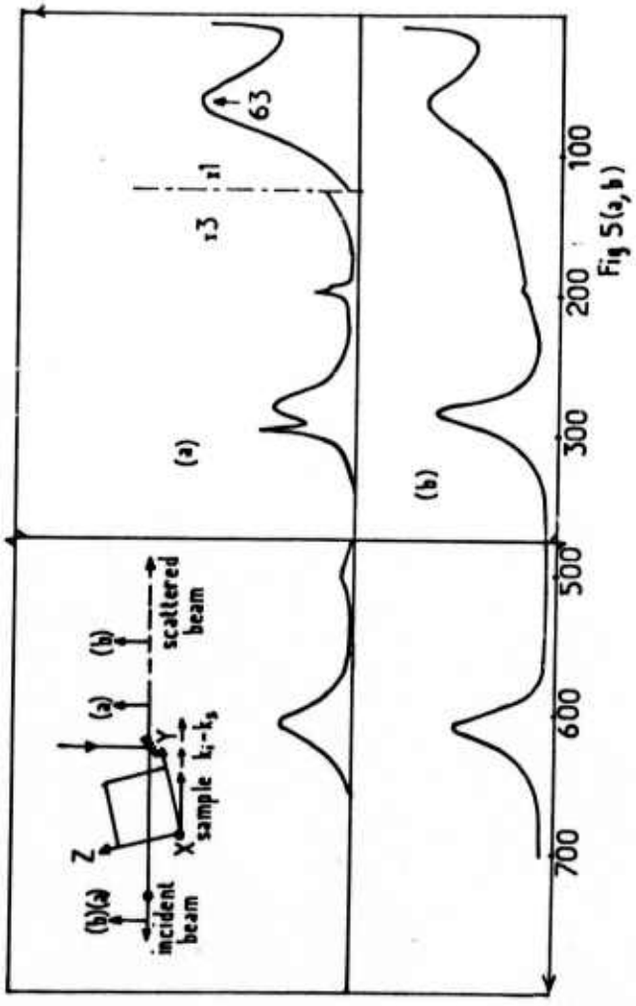
(a)
(b)
63
13
11
100
200
300
500
600
700
scattered beam
incident beam
sample
(a)
(b)
(b)(a)
Z
X
Y

Fig 5(a,b)

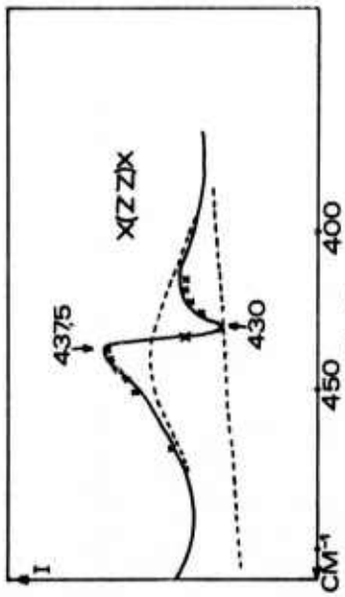

Fig 6

ASSESSMENT OF PYROELECTRIC MATERIALS FOR VIDICON APPLICATIONS

M. I. Bell and P. M. Raccah

Yeshiva University
Physics Department
New York, New York

ABSTRACT

An analysis is made of the physical properties of pyroelectric materials which determine their performance as vidicon targets. Particular attention is paid to three factors: (1) signal-to-noise figure of merit, (2) thermal diffusivity, and (3) target capacitance. It is shown that at room temperature or above, the first two quantities depend on different (essentially unrelated) physical parameters, so that their effects on overall resolution can be treated independently. Examination of the figures of merit relevant to vidicon operation in the anode potential stabilized and cathode potential stabilized modes shows that substantial (order-of-magnitude) improvement over presently available materials is impossible in the first case and highly unlikely in the second.

INTRODUCTION

In selecting a pyroelectric material for use as a vidicon target, three factors directly related to the physical properties of the material must be considered (1). They are: (1) the signal-to-noise figure of merit M(n) in the absence of lateral thermal conduction in the target, (2) the thermal modulation transfer function F, which gives the fractional reduction in available pyroelectric signal due to thermal diffusion, and (3) the target capacitance, which, together with the impedance of the electron beam, determines the extent of image persistence (capacitive lag) caused by incomplete readout of the pyroelectric charge. For operation at or above room temperature, the first two factors can be shown to depend on different physical properties, making it possible to consider them independently. In the case where capacitive lag is the limiting factor in the resolution, its effects can be taken into account by a suitable modification of the figure of merit (1).

FIGURE OF MERIT

The figure of merit of a pyroelectric material used as a vidicon target depends on the method chosen for signal readout (2). The two methods which have been employed to date are anode potential stabilization (APS) and cathode potential stabilization (CPS). The figures of merit for these techniques can be summarized as (1):

$$M(n) = \frac{\alpha \varphi}{\rho c \epsilon^{n} z^{1-n}}, \qquad (1)$$

where α = optical absorption coefficient
φ = pyroelectric coefficient
ρ = density
c = specific heat per gram
$\epsilon = 1+4\pi\chi$ = static dielectric constant
z = target thickness

The value of the exponent depends on the readout mode and amplifier bandwidth Δf:

$$n = \begin{cases} 0 & \text{APS, } \Delta f > 2\text{MHz or CPS, } \Delta f > 1.5\text{ MHz} \\ \frac{1}{2} & \text{APS, } \Delta f < 2\text{MHz} \\ 1 & \text{CPS, } \Delta f < 1.5\text{MHz} \end{cases}$$

The results of Taylor and Boot (2) indicate that the signal-to-noise ratio falls off so rapidly with increasing amplifier bandwidth that only the cases $n = \frac{1}{2}$ and $n = 1$ are likely to be of practical interest with materials currently in use. Operation in the large bandwidth ($n = 0$) mode might be possible with materials having larger pyroelectric coefficients than triglycine sulfate (TGS), but all such materials now known have large dielectric constants and so would suffer from capacitive lag (1). As a result of these considerations, only $M(\frac{1}{2})$ and $M(1)$ will be discussed here.

Since a vidicon target is operated in a closed circuit and at a high modulation (chopping or panning) frequency, the thermodynamic conditions require that the pyroelectric coefficient and specific heat at constant electric field and the adiabatic dielectric constant be used in Eq. (1). Then

$$M(n) = \frac{\alpha \varphi_E}{C_E (4\pi\chi_S)^n z^{1-n}} , \qquad (2)$$

where S is the entropy, $C_E = \rho c_E$ is the volume specific heat, and we have used the fact that $\epsilon \gg 1$ in all cases of interest. The thermodynamic derivatives at constant field (C_E) and constant entropy (χ_S) can be related to their counterparts at constant polarization (C_P) and constant temperature (χ_T) by arguments analogous to those used for systems in which pressure and volume are the thermodynamic variables (3). One obtains the relations

$$C_E/C_P = \chi_T/\chi_S = 1 + X , \qquad (3)$$

where $X = T\varphi_E^2/C_P\chi_T$. The figure of merit is then given by

$$M(n) = \frac{\alpha \varphi_E (1+X)^{n-1}}{C_P (4\pi\chi_T)^n z^{1-n}} , \qquad (4)$$

and for $n = \frac{1}{2}$ we find

$$M(\tfrac{1}{2}) = \alpha (4\pi T C_P z)^{-\frac{1}{2}} \left(\frac{X}{1+X}\right)^{\frac{1}{2}} \qquad (5)$$

Garn and Sharp (1) have used Eq. (1) to evaluate $M(\frac{1}{2})$ from the room-temperature experimental data for a number of crystals, assuming $\alpha = 1$ and a target thickness of $z = 30$ μm. Their results are shown in Fig. 1, plotted as a function of $(X/1+X)^{1/2}$. Figure 1 also gives results based on the data compiled by Garn and Sharp (1) for ceramics and polymers. For the polymers, $M(\frac{1}{2})$ was re-calculated using $z = 30$ μm instead of $z = 6$ μm to permit comparison with the results for ceramics and single crystals. Where necessary, C_E was estimated from measurements on closely related materials.

Figure 1 clearly demonstrates that $M(\frac{1}{2})$ is in fact proportional to $(X/1+X)^{1/2}$, with essentially the same coefficient of proportionality for all materials reported in Ref. 1. Hence Eq. (5) can be written

$$M(\tfrac{1}{2}) = M^*(\tfrac{1}{2}) \left(\frac{X}{1+X}\right)^{\frac{1}{2}} \qquad (6)$$

where

$$M^*(\tfrac{1}{2}) = \alpha(4\pi T C_p z)^{-\frac{1}{2}} \qquad (7)$$

is the theoretical maximum figure of merit since $(X/1+X)^{1/2}$ cannot exceed one. From a least-squares fit to the data in Figure 1, we find that $M^*(\frac{1}{2}) = 20 \pm 2 \times 10^{-8}$ C-cm$^{1/2}$/J. To understand why $M^*(\frac{1}{2})$ as given by Eq. (7) should be effectively independent of the material chosen, we note first that since C_p is defined at constant polarization, it cannot contain any anomalous contribution from the ferroelectric polarization. So in a ferro-electric C_p can be identified with the ordinary lattice specific heat. Now at room temperature the lattice specific heat has very nearly reached its high-temperature limiting value of 3k per particle (k is Boltzmann's constant) in all but the few materials with exceptionally high Debye temperatures. Thus the specific heat per unit volume C_p depends only on the particle density, which is known to have essentially the same value (a few times 10^{22} particles per cubic centimeter) in all solids. If we take the particle density to be one tenth of Avogadro's number per cubic centimeter (i.e. 6×10^{22} cm^{-3}) and again use $T = 300$ K, $\alpha = 1$, $z = 30$ μm, Eq. (7) gives $M^*(\frac{1}{2}) = 20 \times 10^{-8}$ C-cm$^{1/2}$/J, in agreement with the experimental result reported above.

A second, perhaps more important fact to be noted in Fig. 1 is that L-alanine doped TGS (LATGS), the material with highest known value of $M(\frac{1}{2})$, reaches 40% of the theoretical limit $M^*(\frac{1}{2})$. Although this previously unrecognized fact is discouraging from the point of view of attempts to obtain larger absolute values of $M(\frac{1}{2})$, it does demonstrate the remarkable effect that doping or atomic substitution can have on the figure of merit (e.g. compare X = 0.004 for triglycine selenate (TGSe) with X = 0.2 for LATGS). These large variations in X suggest that if a target material is selected for characteristics other than large $M(\frac{1}{2})$ (e.g. small dielectric constant, low thermal diffusivity, or good chemical stability) it may be possible to use substitution or doping to bring $M(\frac{1}{2})$ substantially closer to its theoretical limit.

As noted above, the figure of merit for operation in the CPS mode is not $M(\frac{1}{2})$ but M(1). In addition, it can be shown (1) that if the target is sufficiently thin or the dielectric constant sufficiently high that resolution is limited by capacitive lag, the appropriate figure of merit is M(1), independent of readout mode or amplifier bandwidth. Returning to Eq. (4), we find for n = 1

$$M(1) = \frac{\alpha\varphi_E}{4\pi C_p X_T} \tag{8}$$

If we restrict our attention to ferroelectric crystals, Eq. (8) can be analyzed with the aid of the recently developed generalized molecular field theory of ferroelectricity (4). In this theory the crystal is regarded as an array of N electric dipoles of moment μ which interact via a local field E_ℓ, which is the same at each dipole site and given by

$$E_\ell = E + f(P) , \tag{9}$$

where E is the macroscopic (applied) electric field, and f is an arbitrary odd function of the polarization P. It is readily shown that if the dipoles are free to assume any orientation, then the polarization is given by

$$P/N\mu = (\coth x - 1/x) \tag{10}$$

where

$$x = \mu E_\ell / kT \tag{11}$$

Since $N\mu$ is the largest polarization possible in this model, it can be determined by extrapolating the observed spontaneous polarization to T = 0. Equation (10) can be solved numerically to give x as a function of $P/N\mu$, and the results are shown in Fig. 2.

The generalized molecular field theory also gives

$$\varphi_E/\chi_T = N\mu\lambda x/3T_o \ , \qquad (12)$$

where T_o is the Curie-Weiss temperature and $\lambda = (df/dP)_{P=0}$ is the Lorentz factor. Equations (8) and (12) yield

$$M(1) = \frac{\alpha}{4\pi C_P} \frac{N\mu\lambda}{3T_o} x \ . \qquad (13)$$

Garn and Sharp (1) have used Eq. (1) to evaluate M(1) from the experimental data for a number of ferroelectric crystals, assuming $\alpha = 1$. Working backward from these results for M(1), using experimental values for T_o, $N\mu$, and λ, and estimating C_P as in the case of $M(\frac{1}{2})$, we have used Eq. (13) to determine the value of x, and the corresponding $P/N\mu$ from Eq. (10), needed to account for the observed M(1). The values required, shown in Table I, are quite reasonable, with x always of the order of one and $P/N\mu$ varying from 0.13 for TGSe quite near its Curie temperature to 0.74 for triglycine fluoberyllate (TGFB). For reference purposes we have also listed the experimental values of λ obtained from the relation $\lambda = 4\pi T_o/C$, where C is the Curie constant.

TABLE I

Experimental Values of Parameters in Eq. (13)

	M(1) (10^{-10} C-cm/J)	x	$P/N\mu$	λ
TGS	2.6	1.6	0.46	1.14
TGFB	8.4	3.9	0.74	1.72
TGSe	0.42	0.4	0.13	0.93
$NaNO_2$	3.2	1.3	0.39	0.83
$BaTiO_3$	0.42	2.9	0.66	0.033
$LiTaO_3$	1.2	3.0	0.67	0.070

These results suggest that Eq. (13) can be used to estimate the largest value of M(1) one might reasonably expect to find in a ferroelectric crystal. The Lorentz factor λ is not likely to exceed the value $\lambda = 4\pi/3$ appropriate to point dipoles on a cubic lattice. (No material studied experimentally has been found to have a λ significantly higher than this.) To maximize M(1) at room temperature we must have T_o only slightly higher than 300 K, and for convenience we choose $3T_o = 1000$ K. There is more uncertainty in estimating an upper bound for $N\mu$, but we must note the well-known fact (5) that all known ferroelectrics fall into one of two classes: those with relatively modest spontaneous polarization and Curie constants of the order of 10^3, and those with a larger polarization and Curie constants of the order of 10^5. The latter class, consisting mainly of oxygen-octahedra ferroelectrics like $BaTiO_3$ or $LiTaO_3$, will have Lorentz factors much smaller than $4\pi/3$, and so cannot yield large values of M(1). In terms of the spontaneous polarization, the dividing line between the two classes seems to lie near 10 $\mu C/cm^2$ (5), so we will take this as an estimate of the largest $N\mu$ likely to be found in a material with a large λ. Finally, we take $x = 2$, since Fig. 3 shows this to be within a factor of two of the exact result throughout the range $0.4 < P/N\mu < 0.8$. (Larger values of $N\mu$ are unlikely on the assumption that T_o is only slightly above room temperature.) With these values for the parameters appearing in Eq. (13), one obtains $M(1) = 2.7 \times 10^{-9}$ C-cm/J, or just a factor of three larger than the value for TGFB. Despite considerable uncertainty in this estimate, it seems reasonable to conclude that the existence of a ferroelectric crystal with M(1) an order of magnitude greater than that of TGFB is most improbable: such a material would require properties quite unlike those of any known ferroelectric.

THERMAL DIFFUSION

The thermal modulation transfer function has the form (1)

$$F = F_o\,(1+y^2)^{-\frac{1}{2}} \quad , \tag{14}$$

where F_o and y depend on whether the incident radiation is modulated by chopping or by panning the camera:

$$F_o = \begin{cases} 1, \text{ chopping} \\ \dfrac{\sin\theta}{\theta}, \text{ panning} \end{cases}$$

$$y = \begin{cases} 2\pi\delta N^2/f, \text{ chopping} \\ 2\pi\delta N/v, \text{ panning} \end{cases} \tag{15}$$

where $\theta = \pi N v t_f$,

and δ = thermal diffusivity
N = image resolution
f = chopper frequency
v = panning velocity
t_f = panning time constant

At low resolution ($y \ll 1$) we have $F \simeq 1$ for either form of modulation. The effect of thermal diffusion on resolution can be examined by defining a critical resolution N_c at which F has fallen to some fraction of its low resolution value, where the fraction chosen depends on the contrast reduction at high spatial frequencies which is acceptable in a given application. It is easily shown that

$$N_c \propto \begin{cases} 1/\delta^{\frac{1}{2}}, \text{ chopping} \\ 1/\delta, \text{ panning} \end{cases} \tag{16}$$

demonstrating that while both modulation schemes benefit from reduced thermal diffusivity, the relative improvement is greater for panning. We can now show that in principle F can be increased by reducing δ, i.e. F and M(n) vary independently from one material to another.

The thermal diffusivity is the ratio of the thermal conductivity κ to the specific heat:

$$\delta = \kappa/C_E \quad , \tag{17}$$

and the thermal conductivity can be written as

$$\kappa = C_E v_o \ell = C_E v_o^2 \tau \ , \qquad (18)$$

where v_o is an average phonon velocity and ℓ and τ the average phonon mean free path and scattering time, respectively. In the Debye model (6) v_o is proportional to the Debye temperature Θ. In most crystals at room temperature, τ is dominated by phonon-phonon scattering and can be shown (7) to be proportional to Θ/T. We then have

$$\delta = v_o^2 \tau = A\Theta^3/T, \qquad (19)$$

where the coefficient A is nearly independent of the material chosen (7). The results of the previous section show that although M(n) depends on Θ through C_P, this dependence has practically disappeared at room temperature since T/Θ is then large enough to bring C_P close to its limiting value of 3k per atomic volume. As a result, it is possible in principle to reduce δ without affecting M(n). It is clear from Eq. (19) that materials with low Debye temperatures should be sought, i.e. materials which are "soft" in the sense of having small elastic stiffnesses and low sound velocities. The strong dependence of N_c on Θ suggests that substantial improvements can be made in this way.

CONCLUSIONS

We have considered the influence of the physical properties of pyroelectric materials on their performance as vidicon targets. The signal-to-noise figure of merit $M(\frac{1}{2})$, relevant to anode potential stabilized vidicon operation (and to small area detectors), was found to be subject to a theoretical limit dictated by thermodynamic considerations. This figure of merit can be increased substantially within a family of structurally related materials, but it was shown that presently available materials already realize as much as 40% of the theoretical maximum. The figure of merit M(1), relevant to cathode potential stabilized vidicon operation (and to target-capacitance limited operation in either readout mode) was studied with the aid of recent developments in the theory of ferroelectricity. Although no firm upper limit was obtained for this figure of merit, evidence was presented which indicates that only modest improvement over presently available materials is likely. Analysis of the problem of thermal diffusion shows that materials with low Debye temperatures should be sought and that the relative improvement in resolution obtained in this way is greater if the image is modulated by panning rather than chopping.

ACKNOWLEDGEMENTS

One of the authors (M.I.B.) is grateful to L.E. Garn and B. Singer for helpful discussions. This work was supported by the Defense Advanced Research Projects Agency under contract DAAB 07-74-C-0470.

REFERENCES

(1) L.E. Garn and E.J. Sharp, IEEE Trans. Parts, Hybrids, and Packaging PHP-10, 208 (1974)
(2) R.G.F. Taylor and H.A.H. Boot, Contemp. Phys. 14, 55 (1973).
(3) K. Huang, Statistical Mechanics (Wiley, New York, 1963) pp 21-23.
(4) M.I. Bell and P.M. Raccah, Bull. Am. Phys. Soc. 20, 349 (1975).
(5) F. Jona and G. Shirane, Ferroelectric Crystals (Macmillan, New York, 1962) pp. 13-14.
(6) M. Born and K. Huang, Dynamical Theory of Crystal Lattices (Oxford University Press, New York, 1954) Chap. II.
(7) P.G. Klemens, Solid St. Physics 7, 1 (1958).

Figure Captions

Figure 1. The figure of merit $M(\frac{1}{2})$ from Ref. 1 as a function of the dimensionless variable $(X/1+X)^{1/2}$.

Figure 2. Solutions of the polarization equation $P/N\mu = \coth x - 1/x$.

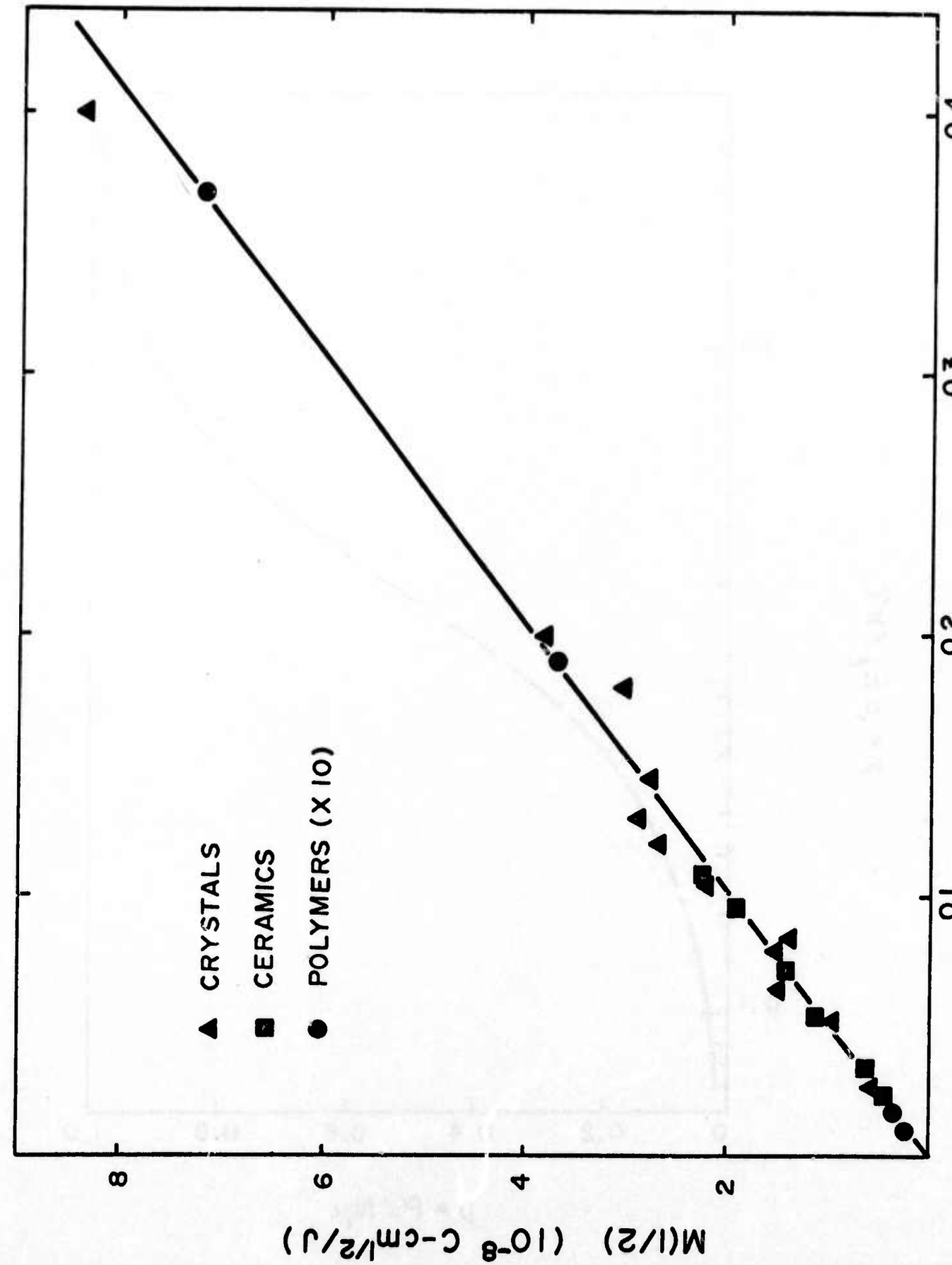
CRYSTALS
CERAMICS
POLYMERS (X 10)
M(1/2) (10⁻⁸ C-cm^1/2/J)
(X/1+X)^1/2
2
4
6
8
0.1
0.2
0.3
0.4

Fig. 1

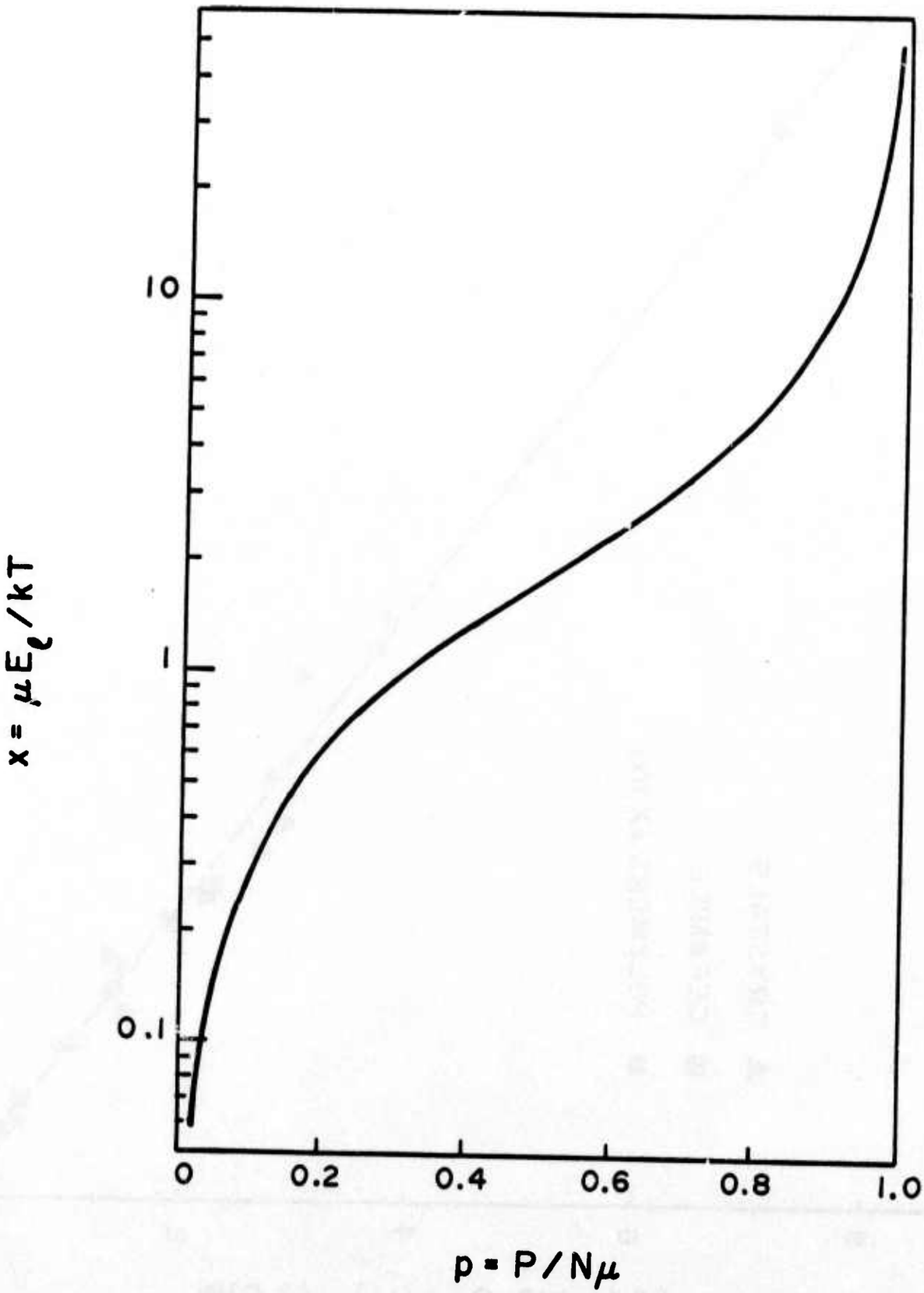

Fig. 2

DISTRIBUTION LIST

101 Defense Documentation Center
ATTN: DDC-TCA
Cameron Station (Bldg 5)
*012 Alexandria, Virginia 22314

107 Director
National Security Agency
ATTN: TDL
001 Fort George G. Meade, MD
20755

108 Director, Defense Nuclear Agy
ATTN: Technical Library
001 Washington, DC 20305

200 Office of Naval Research
Code 427
001 Arlington, VA 22217

203 Naval Ship Engineering Center
ATTN: Code 6179B
Prince Georges Center Bldg
001 Hyattsville, MD 20782

206 Commander
Naval Electronics Lab Ctr
ATTN: Library
001 San Diego, California
92152

207 Commander
US Naval Ordnance Lab
ATTN Technical Library
001 White Oak, Silver Spring, MD
20910

210 Commandant, Marine Corps
Hq, US Marine Corps
ATTN: Code AO4C
001 Washington, DC 20380

212 Communications-Electronics Div
Development Center
Marine Corps Develop & Educ Cmd
001 Quantico, Virginia 22134

217 Naval Air Systems Command
Code: AIR-5336
Main Navy Building
001 Washington, DC 20325

301 Rome Air Development Center
ATTN: Documents Library
(TDLD)
001 Griffiss AFB, New York 13440

307 Hq ESD(TRI)
L. G. Hanscom Field
001 Bedford, MA 01730

309 Air Force Avionics Lab
ATTN: AFAL/DOT, STINFO
002 Wright-Patterson AFB, Ohio
45433

310 Recon Central/RSA
AF Avionics Laboratory
001 Wright-Patterson AFB, Ohio
45433

314 Hq, Air Force Systems Cmd
ATTN: DLTE
Andrews AFB
001 Washington, DC 20331

315 Director
Air University Library
ATTN: AUL/LSE-64-285
001 Maxwell AFB, Alabama 36112

319 Air Force Weapons Laboratory
ATTN: Technical Library (SUL)
001 Kirtland AFB, New Mexico
87117

400 HQDA(DAMI-ZA)
002 Washington, DC 20310

405 Ofc, Asst Sec of the Army (R&D)
ATTN: Asst for Research
Room 3-E-379, The Pentagon
001 Washington, DC 20310

408 HQDA(DARD-ARP/Dr R.B. Watson)
001 Washington, DC 20310

409 Commanding General
US Army Materiel Command
ATTN: DRCMA-EE
5001 Eisenhower Ave.
001 Alexandria, Virginia 22333

* DECREASE TO 2 COPIES IF REPORT IS NOT RELEASABLE TO PUBLIC. SEE ECOMR 70-31 FOR TYPES OF REPORTS NOT TO BE SENT TO DDC.

415 Commanding General
US Army Materiel Command
ATTN: DRCRD-O
5001 Eisenhower Ave.
001 Alexandria, VA 22333

419 Commanding General
US Army Missile Command
ATTN: DRSMI-RR
(Dr. J. P. Hallowes)
001 Redstone Arsenal, Alabama 35809

421 CG, US Army Missile Command
Redstone Scientific Info Ctr
ATTN: Chief, Document Sect
002 Redstone Arsenal, Alabama 35809

423 Commanding General
US Army Weapons Command
ATTN: DRSWE-REF
001 Rock Island, Illinois 61201

426 Commanding Officer
Vint Hills Farm Station
ATTN: Ch, Systems Engrg Div
Opns Center
001 Warrington, Virginia 22186

430 Commanding Officer
US Army Ordnance School
ATTN: ATSOR-CTD
001 Aberdeen Proving Ground, MD 21005

431 Commander
US Army Intelligence School
ATTN: ATSIT-CTD
001 Fort Huachuca, AZ 85613

433 Hq, US Army Aviation Sys Cmd
ATTN: DRSAV-C-AD
P.O. Box 209
001 St. Louis, Missouri 63166

442 Commanding Officer
Harry Diamond Laboratories
ATTN: Library
001 Washington, D.C. 20438

443 CO, USA Foreign Sci & Tech Ctr
ATTN: DRXST-IS1
220 Seventh St, NE
002 Charlottesville, VA 22901

444 CO, USA Foreign Science Div
ATTN: AMXST CE Division
220 Seventh St, NE
001 Charlottesville, Virginia 22901

448 Commanding Officer
Picatinny Arsenal
ATTN: SMUPA-TVI
001 Dover, N. J. 07801

449 Commanding Officer
Picatinny Arsenal
ATTN: SMUPA-RT-S, Bldg 59
002 Dover, N. J. 07801

451 Commanding Officer
Frankford Arsenal
ATTN: L8400 (Dr. W. McNeill)
001 Philadelphia, PA 19137

462 Commanding Officer
US Army Materials and Mech
Research Center
ATTN: DRXMR-ATL Tech Lib Br
001 Watertown, Mass. 02172

463 President
US Army Artillery Board
001 Fort Sill, Oklahoma 73503

464 Commanding Officer
Aberdeen Proving Ground
ATTN: Tech Library, Bldg 313
002 Aberdeen Proving Gr, MD 21005

465 Commanding Officer
Aberdeen Proving Ground
ATTN: STEAP-TL
001 Aberdeen Proving Gr, MD 21005

480 Commanding Officer
USASA Test and Evaluation Cen
001 Fort Huachuca, Arizona 85613

483 US Army Research Office-Durham
ATTN: CRDARD-IP
Box CM, Duke Station
001 Durham, N. C. 27706

484 US Army Research Ofc-Durham
ATTN: Dr. Robert J. Lontz
Box CM, Duke Station
001 Durham, North Carolina 27706

486 Commanding Officer
USA Mobility Eqpt R&D Cen
ATTN: Tech Doc Cen, Bldg 315
002 Fort Belvoir, Virginia 22060

488 USA Security Agency
ATTN: IARD
Arlington Hall Sta, Bldg 420
001 Arlington, Virginia 22212

489 Commanding General
US Army Tank-Automotive Command
ATTN: DRSTA-RH-FL
001 Warren, Michigan 48090

492 Commandant
US Army Air Defense School
ATTN: C&S Dept, MSL Sci Div
001 Fort Bliss, Texas 79916

493 Director
USA Engr Waterways Exper Sta
ATTN: Research Center Library
002 Vicksburg, Mississippi 39180

495 CG, Deseret Test Center
ATTN: STEPD-TT-ME(S) Met Div
Bldg 103, Soldiers Circle
001 Fort Douglas, Utah 84113

500 Commanding Officer
Yuma Proving Ground
ATTN: STEYP-AD (Tech Lib)
001 Yuma, Arizona 85364

501 Commanding Officer
US Army Arctic Test Center
002 APO, Seattle 98733

502 CO, USA Tropic Test Center
ATTN: STETC-MO-A (Tech Lib)
Drawer 942
001 Fort Clayton, Canal Zone 09827

503 Director
US Army Adv Matl Concepts Agcy
ATTN: DRXCD
001 Washington, D. C. 20315

504 Commanding General
US Army Materiel Command
ATTN: DRCRD-R
5001 Eisenhower Ave.
001 Alexandria, VA 22333

512 Commanding Officer
USACDC Armor Agency, ATTN: ATSAR-CTD
001 Fort Knox, Kentucky 40121

516 Commandant
US Army Field Artillery School
ATTN: Target Acquisition Dept
002 Fort Sill, Oklahoma 73503

517 Commanding General
US Army Missile Command
ATTN: DRSMI-RFG (Mr N. Bell)
001 Redstone Arsenal, Ala. 35809

518 Commanding Officer
Harry Diamond Laboratories
ATTN: DRXDO-RCB (Mr. Nemarich)
001 Washington, D. C. 20438

596 Commanding Officer
US Army Southeastern Signal School
ATTN: ATSN-CTD-MS
001 Fort Gordon, GA 30905

598 Commanding Officer
USA Satellite Comm Agency
ATTN: DRCPM-SC-3
001 Fort Monmouth, N. J. 07703

599 Tri-Tac Office
ATTN: TT-D (Dr. Pritchard)
001 Fort Monmouth, N. J. 07703

607 Commanding General
USA Tank-Automotive Command
ATTN: DRSTA-Z, Dr. J. Parks
001 Warren, Michigan 48090

610 Director
Night Vision Lab (USAECOM)
ATTN: DRSEL-NV-D
001 Fort Belvoir, Virginia 22060

614 Chief
Ofc of Missile Electronic Warfare
Electronic Warfare Lab, ECOM
001 White Sands Missile Range, NM
88002

616 CG, USA Electronics Command
ATTN: DRSEL -PP/P-IED
(Mr. C. Mogavero)
225 South 18th Street
001 Philadelphia, PA. 19103

617 Chief, Intel Materiel Dev & Support
Ofc, Electronic Warfare Lab, (ECOM)
001 Fort Meade, MD 20755

680 Commanding General
US Army Electronics Command
000 Fort Monmouth, N. J. 07703

1DRSEL-NV-D
1DRSEL-NL-D
1DRSEL-WL-D
1DRSEL-VL-D
1DRSEL-CT-D
1DRSEL-BL-D
1DRSEL-TL-DT
6DRSEL-TL-ES
(Ofc of Record)
1DRSEL-TE

2DRSEL-MS-TI
1DRSEL-GG-TD
1DRSEL-EN
1DRSEL-PA
1USMC-LNO
1 DRSEL-PP-C-ES-1

1DRSEL-RD
1DRSEL-TL-D
{ ECOM Technical reports only

703 NASA Sci & Tech Info Facility
ATTN: Acquisitions Br(S-AK/DL)
P.O. Box 33
002 College Park, Maryland 20740

705 Advisory Gp on Electron Devices
201 Varick St. 9th Floor
002 New York, New York 10014

706 Advisory Gp on Electron Devices
ATTN: Secy, Sp Gr on Opt Masers
201 Varick Street
002 New York, New York 10014

708 Ballistic Msl Radiation Anal Cen
Univ of Mich., Willow Run Lab
Institute of Science & Tech
001 PO Box 618, Ann Arbor, Michigan
48107

711 Metals and Ceramics Inf Center
Battelle
505 King Avenue
001 Columbus, Ohio 43201

712 Elec Properties Info Center
Hughes Aircraft Company
Centinela and Teale Streets
001 Culver City, California 90230

715 Plastics Tech Eval Center
Picatinny Arsenal, Bldg 3401
001 Dover, N. J. 07801

717 Reliability Analysis Center
Rome Air Development Center
ATTN: J.M. Schramp/RCRM
001 Griffiss AFB, New York 13440

718 Remote Area Confligt Info Ctr
Battelle Memorial Institute
505 King Avenue
001 Columbus, Ohio 43201

719 Shock and Vibration Info Center
Naval Research Lab (Code 6020)
001 Washington, D. C. 20390

* Or number specified in contract. Add COTR's mail symbol.

720 Thermophysical Properties Res Ctr
Purdue Univ., Research Park
2595 Yeager Road
001 Lafayette, Indiana 47906

721 Vela Seismic Info Center
University of Michigan
Box 618
003 Ann Arbor, Michigan 48107

Department of Electrical Engineering
ATTN: Dr. A. van der Ziel
University of Minnesota
001 Minneapolis, MN 55455

Dr. George Heilmeier
Director, Advanced Research
Project Agency
1400 Wilson Blvd.
002 Arlington, VA 22209

Commander
US Army Combined Arms Combat
Developments Activity
ATTN: ATCAIC
001 Fort Leavenworth, KS 66027

Commander
US Army Training & Doctrine Command
ATTN: ATCD-CI
001 Fort Monroe, VA 23651

Director
Naval Research Laboratory
CODE 2627
001 Washington, DC 20390

Commander
US Army R&D Group
(Far East)
003 APO, San Francisco, CA 96343

Commandant
US Army Engineer School
ATTN: ATSEN-CTD
001 Fort Belvoir, VA 22060

Commanding General
US Army Materiel Command
ATTN: DRSEL-TP (Dr. B. Zarwyn)
5001 Eisenhower Ave.
001 Alexandria, VA 22333

Institute of Science & Tech
The University of Michigan
P.O. Box 618 (IRIA Library)
001 Ann Arbor, MI 48107

Director, Night Vision Laboratory
US Army Electronics Command
ATTN: DRSEL-NV-FIR (Dr. R. Ennulat)
001 Fort Belvoir, VA 22060

Director, Night Vision Laboratory
US Army Electronics Command
ATTN: DRSEL-NV-D (Mr. Edward C. Walker)
001 Fort Belvoir, VA 22060